



Remote sensing of atmospheric aerosol using spaceborne optical observations

A.A. Kokhanovsky

Institute of Environmental Physics, University of Bremen, D-28334 Bremen, Germany

ARTICLE INFO

Article history:

Received 4 September 2011

Accepted 31 October 2012

Available online 9 November 2012

Keywords:

Aerosol

Pollution

Radiative transfer

Light scattering

Remote sensing

Satellite

ABSTRACT

The overview of modern satellite aerosol remote sensing algorithms, corresponding instrumentation, and global aerosol properties is presented. It is shown that the accuracy of retrievals increases, if multi-angular or/and polarimetric measurements in broad spectral intervals are performed.

© 2012 Elsevier B.V. All rights reserved.

Contents

| | |
|--|-----|
| 1. Introduction | 95 |
| 2. Microphysical and optical properties of atmospheric aerosol | 96 |
| 2.1. Aerosol types | 96 |
| 2.2. Local optical characteristics of aerosol particles | 96 |
| 2.3. Radiative characteristics of aerosol layers | 97 |
| 2.4. The surface reflectance. | 98 |
| 2.5. The inverse problem. | 100 |
| 3. Satellite instruments and algorithms used for aerosol optical thickness retrievals. | 101 |
| 3.1. Spectral top-of-atmosphere reflectance observations. | 101 |
| 3.2. Cloud screening | 103 |
| 3.3. Dual view and multi-angular observations | 104 |
| 3.3.1. AATSR | 104 |
| 3.3.2. MISR | 105 |
| 3.4. Multiangular spectropolarimetry | 105 |
| 3.5. Hyperspectral instruments | 106 |
| 3.6. Spaceborne lidar systems | 106 |
| 4. Future missions | 106 |
| 5. Conclusions | 107 |
| Acknowledgements | 107 |
| References | 107 |

1. Introduction

Atmospheric aerosol is composed of solid and liquid particles suspended in the atmosphere. Water droplets and ice crystals in clouds

and mist are usually not included in the notion of atmospheric aerosol. In some cases it is difficult to distinguish atmospheric aerosol from clouds (Koren et al., 2007, 2008). In particular, water droplets originate from the condensation of water vapor on small aerosol particles and, therefore, it is uncertain in some cases to specify if we deal with a cloud or with wet aerosol.

E-mail address: alexk@iup.physik.uni-bremen.de.

As a matter of fact, for remote sensing applications all particles suspended in the atmosphere must be treated simultaneously without a separation on aerosol and cloud particles. The general task is to derive the chemical composition, concentration and size distributions of particles using various remote sensing techniques (e.g., optical observations from a satellite). This is because aerosol and cloud particles (and also atmospheric gases) do not exist in separation but rather interact on all spatial and time scales.

In this review, we address the question of atmospheric aerosol studies from a satellite using passive solar techniques (Kaufman et al., 1997a,b; King et al., 1999; Kokhanovsky and de Leeuw, 2009; Lee et al., 2009). The problem is formulated as follows: given the characteristics of the optical instrument orbiting the planet and also illumination/observation geometry, is it possible to derive columnar aerosol optical and microphysical properties and also their vertical distributions and aerosol layering? The answer to this question is of relevance to many branches of modern science and technology including environment protection and monitoring, climate change due to anthropogenic aerosol, human health issues, atmospheric vision, image transfer, atmospheric correction, particulate matter transfer between continents (e.g., dust storms) and pollution of atmosphere by natural and man-made aerosol. The discussion of main methods to derive the aerosol properties from a satellite is a main task of this review.

Current satellite observation techniques rely on the assumption that a satellite ground scene (pixel) contains no clouds. Therefore, clear pixels must be selected in advance of retrievals. The additional removal of cloud-contaminated pixels during the post-processing is used as well for the enhancement of accuracy of retrievals. Sub-pixel clouds and also neighboring clouds reduce the quality of derived information on aerosol microphysical and optical characteristics. This is because clouds and underlying surfaces (and not aerosol) dominate the signal as detected on a satellite in many cases (e.g., over land). This feature can be easily observed by a naked eye while flying an aircraft. Clouds and terrestrial surface are readily observed but not aerosols (with exclusions of some rare events such as smoke plumes, volcanic eruptions, oil and wild fires, dust outbreaks, technological catastrophes, etc.).

The review is composed of several sections. In the next section we briefly consider aerosol types and their microphysical, optical and radiative properties. We consider modern retrieval techniques including multi-angle polarimetric observations in Section 3. The last section is devoted to the discussion of future satellite missions aimed at aerosol remote sensing from space.

2. Microphysical and optical properties of atmospheric aerosol

2.1. Aerosol types

Generally, there are three mechanisms for the generation of various aerosol particles in terrestrial atmosphere: (1) aerosol generated from the surface of the planet (e.g., road and desert dust and sea salt), (2) aerosol generated in atmosphere from gaseous phase (e.g., aerosol nucleation bursts), and (3) aerosol of cosmic origin. The flux of particulate matter from space is not negligible and plays some role in the physics and chemistry of upper atmospheric layers (e.g., in mesosphere). However, the tropospheric aerosol properties are clearly dominated by the contribution of various aerosol particles generated at the surface of the planet. They include (1) oceanic aerosol with several fractions including sea salt and organic matter; and (2) continental aerosol composed of suspended dust particles consisting of mixtures of various minerals, soot (brown and black carbonaceous material), biological matter (pollen, spores, and bacteria), particles of volcanic origin, organic, sulfate and nitrate aerosols. There is a tendency of general increase in the atmospheric aerosol load due to human activity, which includes the industrial and agricultural production chains, the operation of various transport systems on the surface, sea, and air. Pollution of air by various condensed matter (and also by hazardous gases such as ozone, and

sulphuric and nitrous oxides, etc.) is a major problem for many urban agglomerations (e.g., Beijing, Calcutta, Cairo, and Moscow). In particular, the link between the concentration of particulate matter in atmosphere and various diseases and mortality is known for a considerable time (van Zelm et al., 2008). This is related to the fact that fine mode particles (with radii, say, below 100 nm) can penetrate to the pulmonary alveoles and remain there causing various health problems and diseases.

The important parameters of aerosol particles are their size, shape, structure (homogeneous or inhomogeneous particles), and chemical composition (Kokhanovsky, 2008). Optical properties of aerosols are determined by their microphysical properties and spectral refractive index. It is a common practice in satellite aerosol remote sensing to consider atmospheric aerosol as a mixture of various components composed of spherical particles. The parameters of lognormal particle size distribution (PSD)

$$f(a) = \left(\sqrt{2\pi}as\right)^{-1} \exp\left[-0.5s^{-2} \ln^2(a/a_0)\right] \quad (1)$$

are specified for each component. Here a is the radius. The parameter of the width of the PSD s is usually in the range 0.5–2.0 and the median radius a_0 is close to 0.1 μm for the fine mode and 1.0 μm for the coarse mode of atmospheric aerosol (Kokhanovsky, 2008). The real part of refractive index is usually in the range 1.3–1.6, depending on the substance and the wavelength. The imaginary part is smaller than 0.01. So aerosol particles only weakly absorb incoming solar light in most cases. However, they strongly scatter light and this scattering is usually inversely proportional to the wavelength λ . So one can see that light scattering by suspended aerosol matter is less spectrally selective as compared to molecular scattering, which is proportional to λ^{-4} . The measurements at shorter wavelengths are more sensitive to the presence of aerosols. So aerosol remote sensing is performed using UV–near IR spectral range in most of cases.

2.2. Local optical characteristics of aerosol particles

Important optical properties of atmospheric aerosol are extinction and absorption coefficients and also phase function, which describes the angular distribution of scattered light. It follows for the extinction coefficient:

$$k_{\text{ext}} = \sum_{j=0}^M N_j C_{\text{ext},j}, \quad (2)$$

where N_j is the number concentration of aerosol particles of j -type, and $C_{\text{ext},j}$ is their average extinction cross section. The value of N_j is related to the dimensionless volumetric concentration of particles w_j as: $w_j = N_j v_j$. Here v_j is the average volume of particles of the j th aerosol type. In a similar way the aerosol absorption coefficient is defined:

$$k_{\text{abs}} = \sum_{j=0}^M N_j C_{\text{abs},j}, \quad (3)$$

where $C_{\text{abs},j}$ is the average absorption cross section.

For large dust particles (much larger than the wavelength of incident light), it follows approximately:

$$C_{\text{ext}} = 2\sigma, \quad (4)$$

where σ is the average geometrical cross section of particles. The value of σ in Eq. (4) is equal to $\pi\langle a^2 \rangle$ for spheres, where brackets here and below mean averaging with respect to the PSD:

$$\langle a^2 \rangle = \int_0^\infty a^2 f(a) da. \quad (5)$$

We can derive for the extinction coefficient of dust particles (see Eqs. (2), (4), and (5)):

$$k_{\text{ext}} = \frac{3w}{2a_{\text{ef}}}, \quad (6)$$

where $a_{\text{ef}} = 3v/4\sigma$ is the effective radius of aerosol particles and w is the volumetric concentration of particles. It follows for spheres: $a_{\text{ef}} = \langle a^3 \rangle / \langle a^2 \rangle$. One derives using Eq. (1): $a_{\text{ef}} = a_0 \exp(2.5s^2)$, if the integration is performed from 0 to infinity. In most of cases it is advised to make integration in the range 0.05–15 μm because smaller and larger particles cannot reside in atmosphere for a long time (due to coagulation and deposition processes).

The single particle absorption and extinction cross sections c_{abs} and c_{ext} can be calculated using Mie theory for spheres if the complex refractive index of particles $m = n - i\kappa$ and also their size distribution are known (Kokhanovsky, 2008). The average cross sections are found after evaluation of integrals similar to Eq. (5). For instance, it follows for the average extinction coefficient (Kokhanovsky, 2008):

$$C_{\text{ext}} = \int_0^\infty c_{\text{ext}}(a)f(a)da. \quad (7)$$

Such an averaging must be done for each aerosol component. The phase function of the aerosol mixture is found as

$$p(\theta) = \frac{\sum_{j=1}^M k_{\text{sca},j} p_j(\theta)}{\sum_{j=1}^M k_{\text{sca},j}}. \quad (8)$$

Here $k_{\text{sca},j}$ is the aerosol scattering coefficient equal to the difference of extinction and absorption coefficients. The phase function of the j th component $p_j(\theta)$ is found via application of Mie theory with subsequent evaluation of averages. In case if polarization properties of aerosol media are of interest, the 4-dimensional phase matrix $\hat{P}(\theta)$ is used:

$$\hat{P}(\theta) = \frac{\sum_{j=1}^M k_{\text{sca},j} \hat{P}_j(\theta)}{\sum_{j=1}^M k_{\text{sca},j}}. \quad (9)$$

This matrix describes the change of the Stokes vector of incident light due to scattering processes in unit volume of atmospheric air (the volume must be sufficiently small so the effects of multiple scattering can be neglected).

2.3. Radiative characteristics of aerosol layers

The aerosol scattering and extinction coefficients change with height above surface, usually being smaller in higher atmospheric layers. However, in many cases distinct aerosol layers can be present at different heights in atmosphere. The altitude of such layers is easily detected studying lidar returns. An example is shown in Fig. 1, where several aerosol layers and their vertical stratification are clearly seen. This information is of immediate importance (say, for aircraft safety and warning systems). The radiometers unlike lidars, which provide information on vertical structure of atmosphere, give information in horizontal direction (see Fig. 2). The determination of aerosol altitudes with multi-angular radiometers and hyperspectral measurements is also possible. However, the inversion procedures are more involved as compared to the analysis of lidar returns and also results are less accurate.

For practical applications and also for purpose of aerosol remote sensing from space it is often assumed that all aerosol is contained in

lower atmospheric layer (say, 0–1 km layer, which is clearly not the case for measurements shown in Figs. 1 and 2). In addition to scattering of light by aerosol particles, one needs to account for height-dependent molecular scattering and absorption. Molecular scattering is of particular importance in UV part of electromagnetic spectrum, where remote sensing of aerosol from space has some advantages (low or negligible surface reflectance, which is not the case in the visible and near infrared for land underlying surfaces). In the near infrared, molecular scattering is low. Note that aerosol remote sensing is usually performed in the near infrared range of the electromagnetic spectrum in case of oceanic underlying surface because the surface reflectance is very low then. In all cases channels free (or almost free) of gaseous absorption are used. For some channels, absorption by ozone and water vapor must be taken into account. The simplest way to account for gaseous absorption is to divide the measured top of atmosphere reflectances $R_{\text{mes}}(\vartheta_0, \vartheta, \varphi)$ by spectral transmittivities depending on the spectral absorption optical thicknesses of corresponding gases. Here ϑ_0 , ϑ , and φ are the solar zenith angle (SZA), viewing zenith angle (VZA), and relative azimuthal angle (RAA), respectively. The zenith angles are counted from the nadir direction. There are different definitions of RAA. In satellite data it is often assumed that the case ($\vartheta_0 = \vartheta$, $\varphi = \pi$) corresponds to the forward scattering direction (glint). In radiative transfer (RT) theoretical studies (see, e.g., Rozanov et al., in preparation), this case corresponds to back-scattering direction. This is an important point to remember in applications of RT codes to the interpretation of satellite measurements. The RT codes provide the intensity of reflected, transmitted, or internal light characteristics for any layer in atmosphere. The corresponding angular distributions are found from the solution of the RT equation, which can be presented in the following form in the scalar case (electromagnetic nature of light being ignored):

$$\mu \frac{dI(\tau)}{d\tau} = B_1(\tau) + B_0(\tau) - I(\tau), \quad (10)$$

where I is the intensity of the diffuse light, μ is the cosine of the zenith angle specifying the direction of propagation (positive value of μ for downward direction), $\tau = k_{\text{ext}}z$, z is the vertical coordinate, and we omitted the angular variables ($\vartheta_0, \vartheta, \varphi$) in the corresponding functions. The total reflected or transmitted light intensity coincides with the diffuse intensity for all directions except the forward scattering direction, where the direct attenuated light intensity must be added. In the case of underlying black surface it is assumed that no diffuse radiation enters the layer neither from below nor from above. Then Eq. (10) can be solved analytically and the result for the intensity of upward radiation at the upper boundary of aerosol layer of optical thickness τ_0 is

$$I(\tau) = \int_0^{\tau_0} \exp(-\tau/\mu) B_1(\tau) d\tau + \int_0^{\tau_0} \exp(-\tau/\mu) B_0(\tau) d\tau, \quad (11)$$

which can be evaluated analytically in case, where analytical results for the source functions $B_0(\tau)$ and $B_1(\tau)$ are known. $B_0(\tau)$ is the source function for singly scattered light and can be presented in the following way (Kokhanovsky, 2008):

$$B_0(\tau) = \frac{\omega_0 F_0}{4\pi} p(\cos\theta) \exp(-\tau/\mu_0), \quad (12)$$

where $\omega_0 = k_{\text{sca}}/k_{\text{ext}}$ is the single scattering albedo, F_0 is the solar irradiance at the unit area perpendicular to the solar beam and positioned at the top of atmosphere, μ_0 is the cosine of the solar zenith angle, $p(\cos\theta)$ is the phase function, $\cos\theta = -\mu\mu_0 + s s_0 \cos\varphi$ is the cosine of scattering angle for the reflected light, $s = \sin\vartheta$, $s_0 = \sin\vartheta_0$.

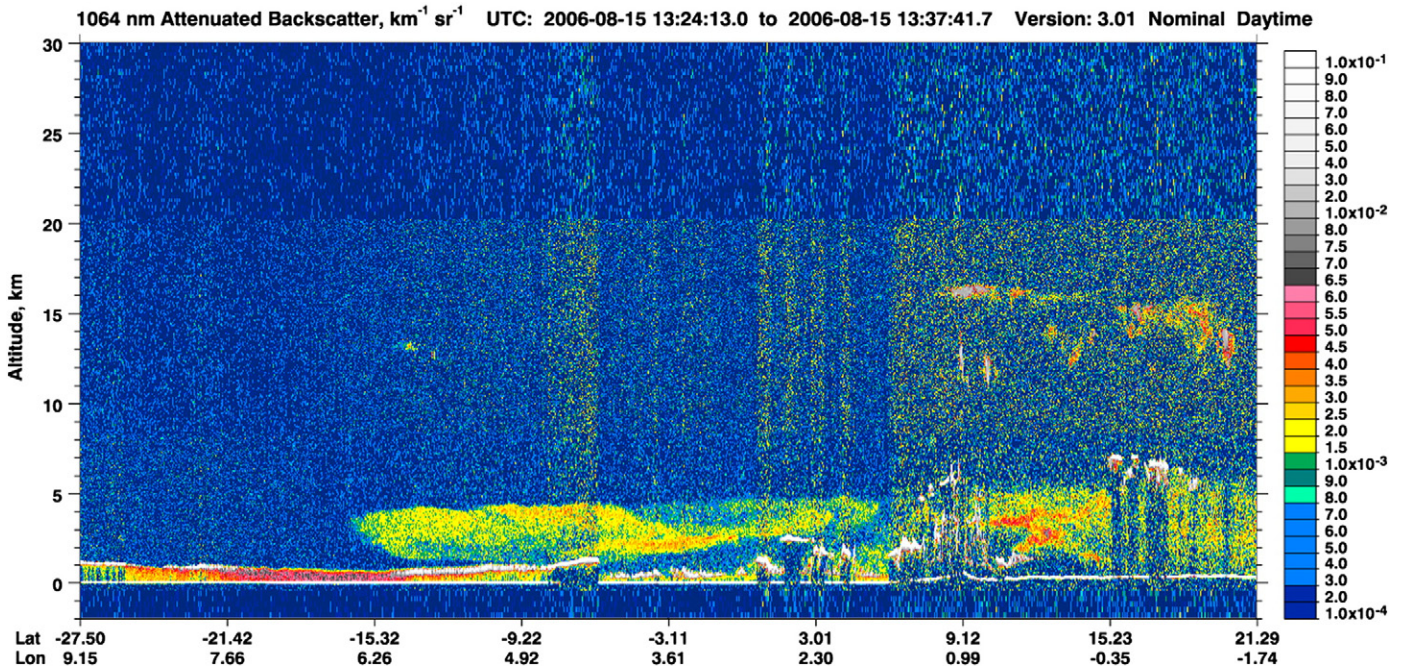


Fig. 1. The 1064 nm attenuated backscatter of CALIPSO.
Courtesy of CALIPSO team, http://www-calipso.larc.nasa.gov/products/lidar/browse_images/show_calendar.php.

In the case of thin aerosol layers, the source function $B_1(\tau)$ due to multiple scattering can be ignored. This enables the derivation of the following equation for the contribution of singly scattered light to the registered signal on a satellite:

$$I_{ss}(\tau) = \frac{\omega_0 p(\cos\theta) \mu_0 F_0}{4\pi(\mu + \mu_0)} (1 - \exp(-\tau_0(1/\mu_0 + 1/\mu))) \quad (13)$$

in absence of contribution from underlying surface (black surface assumption). Neglecting molecular scattering contribution one derives from Eq. (13) for the aerosol optical thickness (AOT):

$$\tau_0 = \frac{1}{M} \ln \left[1 - I_{ss}(\tau) \left\{ \frac{4\pi(\mu + \mu_0)}{\omega_0 p(\cos\theta) \mu_0 F_0} \right\}^{-1} \right], \quad (14)$$

where $M = 1/\mu_0 + 1/\mu$. It follows from this equation that AOT can be retrieved only if the product $\omega_0 p(\cos\theta)$ is known. In some retrievals average values of the single scattering albedo and phase function for a given region are used, which can lead to biases in retrievals in case of aerosol disturbances (smoke, fires, dust outbreaks, aerosol nucleation bursts and humidification effects). The AOT is related to the vertical aerosol columnar mass (Rohen et al., 2011).

The contribution of multiple scattering effects can be significant for thick aerosol layers and then the integral

$$I_{ms}(\tau_0) = \int_0^{\tau_0} \exp(-\tau/\mu) B_1(\tau) d\tau. \quad (15)$$

must be evaluated, which is usually done either approximating function $B_1(\tau)$ or solving corresponding integral equation for the source function $B_1(\tau)$ (Sobolev, 1975). Often the function $I_{ms}(\tau_0)$ is tabulated for various values of τ_0 and also angles $(\vartheta_0, \vartheta, \varphi)$ for the assumed phase function and single scattering albedo and then the minimization procedure is used to find the value of τ_0 , which gives the minimal deviation of calculated and measured reflected solar light intensity for given wavelengths and

viewing directions. In principle, doing so for each satellite channel, one can derive the spectral aerosol optical thickness. As a matter of fact even more elaborated procedures involving multi-angular and polarization measurements are performed, which also enables the assessment of aerosol phase function and single scattering albedo (aerosol model) from the measurements itself. There are no absolutely black underlying surfaces and there is often a large contribution from underlying surface to the satellite signal. This contribution must be removed in some way before (or derived simultaneously with) spectral aerosol optical thickness retrieval (Katsev et al., 2010).

2.4. The surface reflectance

In the case of underlying non-black surfaces, the notion of the bi-directional reflection distribution function (BRDF) is used. It is defined as

$$\text{BRDF}(\vartheta_0, \vartheta, \varphi) = \frac{I^\dagger}{\mu_0 F_0}, \quad (16)$$

where I is the intensity of light reflected from the surface.

The reflectance is defined as $R = \frac{\pi I^\dagger}{\mu_0 F_0}$ and, therefore, $R = \pi \text{BRDF}$. The radiative transfer problem is formulated using Eq. (10), where

$$B_1(\tau) = \frac{\omega_0}{4\pi} \int_0^{2\pi} d\varphi \int_0^1 \mu' d\mu' p(\cos\theta) I(\mu, \mu', \varphi), \quad (17)$$

and the boundary condition at the lower boundary (surface) is given by the following integral:

$$I^\dagger(\tau = \tau_0) = \pi^{-1} \int_0^1 \mu' d\mu' \int_0^{2\pi} d\varphi' R_s(\mu, \mu', \varphi, \varphi') I_1(\mu', \varphi'). \quad (18)$$

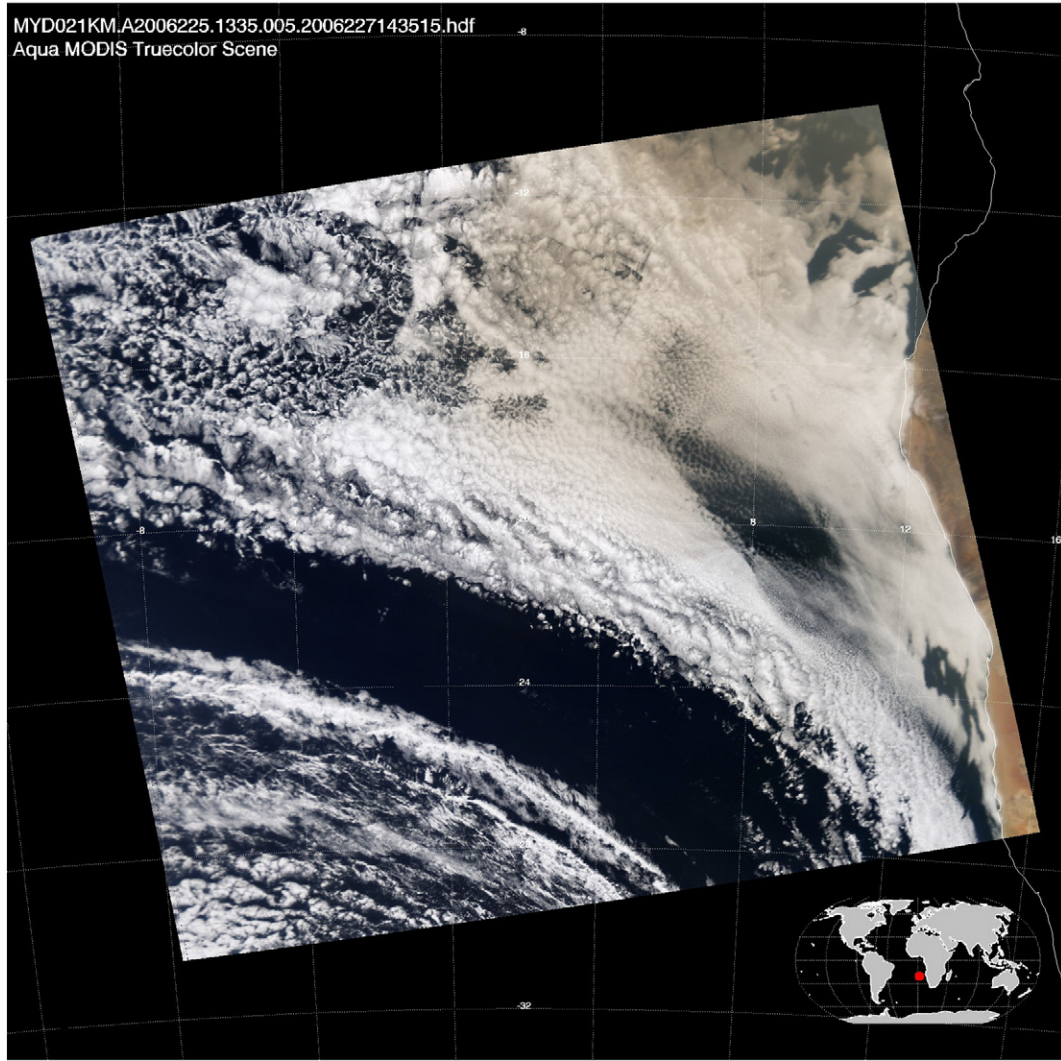


Fig. 2. The MODIS browse image of cloud contaminated by biomass burning aerosol. Courtesy of NASA.

For the Lambertian underlying surface with albedo A , it follows that $R_s(\mu, \mu', \varphi, \varphi') = A = \text{const}$ and the integral is simplified:

$$I^{\uparrow}(\tau = \tau_0) = A\pi^{-1} \int_0^1 \mu' d\mu' \int_0^{2\pi} d\varphi' I_1(\mu', \varphi'). \quad (19)$$

As a matter of fact, the case of the Lambertian underlying surface can be reduced to a simple case of a black underlying surface.

In particular, one can derive for the top of atmosphere reflectance (Sobolev, 1975):

$$R = R_b + \frac{tA}{1-rA}, \quad (20)$$

where R_b represents the atmospheric reflectance at $A=0$, r is the spherical albedo of atmosphere and t is the total atmospheric transmissivity on the way from the top of atmosphere to the surface and then from the surface to satellite. It includes both direct and diffuse light components. The values of R_b , r and t can be calculated and tabulated once for the case of $A=0$ and then used in combination with Eq. (20) to find R at arbitrary Lambertian surface albedo.

The results of calculations at different values of surface albedo are given in Fig. 3 as the function of aerosol optical thickness. It follows

that at some surface albedos, the sensitivity of the reflectance to AOT is very much reduced. Those values of albedo (called critical albedo A_c) make it difficult to perform corresponding retrievals of AOT although they make it possible to estimate single scattering albedo and, therefore, level of atmospheric absorption (Castanho et al., 2008). The value of A_c can be found from Eq. (20) and the condition that

$$\frac{\partial R(A_c)}{\partial \tau} = 0, \quad (21)$$

which gives:

$$A_c = \Lambda \left[\sqrt{1+s} - 1 \right], \quad (22)$$

where

$$\Lambda = d_2/2d_1, s = 4c_1(rc_2 - c_1r^2 - tc_3)/(c_2 - 2rc_1), d_1 = c_1r^2 - rc_2 + tc_3, d_2 = c_2 - 2rd_3 \quad (23)$$

and we introduced the derivatives

$$c_1 = \frac{\partial R_b}{\partial \tau}, c_2 = \frac{\partial t}{\partial \tau}, c_3 = \frac{\partial r}{\partial \tau}. \quad (24)$$

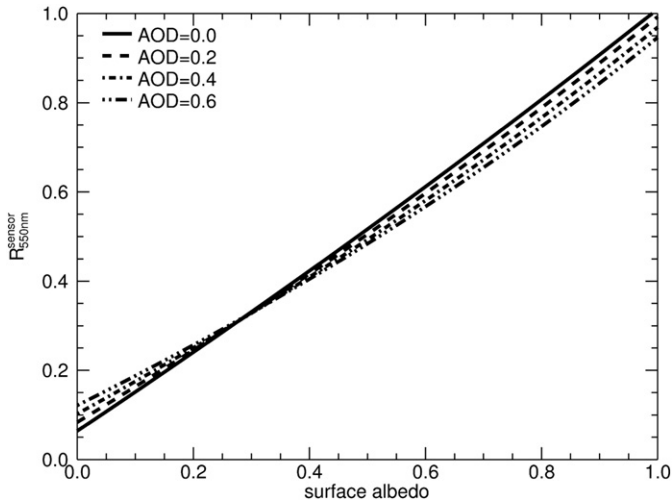


Fig. 3. The dependence of the top-of-atmosphere reflectance on the surface albedo for several AOTs (550 nm) (Seidel et al., 2012).

Clearly, A_c depends both on the phase function and single scattering albedo. In some angular regions, the phase function does not change considerably (Kokhanovsky, 1998). This makes it possible to derive the aerosol single scattering albedo over targets, which have desired underlying surface albedo close to the critical one. These targets can be natural or artificially created. One of such approaches is described by Castanho et al. (2008), who assume that the measured top-of-atmosphere reflectance can be modeled as ($rA \approx 0$, see Eq. (20))

$$R_{clear} = R_{b,clear} + t_{clear}R_s, \quad (25)$$

$$R_{pol} = R_{b,pol} + t_{pol}R_s, \quad (26)$$

for polluted (pol) and clear day. In the case of critical reflectance $R_s \equiv A_c$, we have: $R_{clear} = R_{pol}$ and, therefore,

$$A_c = \frac{R_{b,pol} - R_{b,clear}}{t_{clear} - t_{pol}}. \quad (27)$$

Also we can write for the case of critical surface reflectance:

$$R_{pol} = (R_{b,pol} - BR_{b,clear}) + BR_{clear}, \quad (28)$$

where $B = t_{pol}/t_{clear}$. This equation can be used to estimate AOT. It can be written for several observation directions and wavelengths providing important constrains for the inverse problem solution. Importantly, Eq. (28) does not contain the characteristics of the underlying surface. This equation suggests that the reflectance at a given location on polluted days is linearly proportional to the reflectance on the clear day ($R_{pol} = a + bR_{clear}$, $a = R_{b,pol} - t_{pol}R_{b,clear}/t_{clear}$, and $b = t_{pol}/t_{clear}$). Therefore, the parameters (a and b) can be directly estimated from the measurements itself and then used in the inverse problem solution.

The surface albedo depends on the wavelength. Some examples of the spectral surface reflectance are given in Fig. 4. It follows from this figure that the spectral behavior of the soil and grass surface reflectances differ considerably. This can be used to distinguish both types of surface using spaceborne observations.

The mixed pixel reflectance can be approximately found using the linear combination of, say, bare soil and vegetation spectra:

$$R_s = cR_{veg} + (1-c)R_{soil} \quad (25)$$

with c being the vegetation percentage in the pixel. The accuracy of this approximation depends on the size of the pixel, the value of c and also on the wavelength.

The surface reflectance of a given ground scene depends not only on the wavelength but also on the illumination and viewing geometry. Several models of the angular structure of reflected light were proposed up to date (Pinty et al., 2000; Maignan et al., 2004; Bréon and Vermote, 2012). The reflectance distribution function model for the grass is shown in Fig. 5 ($\vartheta_0 = 60^\circ$). The hot spot characteristic for vegetation is clearly seen in the backward scattering direction. Clearly, this direction must be avoided in aerosol remote sensing applications.

2.5. The inverse problem

There are various possibilities of the inverse problem solution based on Eq. (20). In particular, one can use an approach based on the minimization of the following function:

$$\Psi(\tau_0) = \left\| R_{mes}(\lambda) - R_b(\tau_0(\lambda)) - \frac{t(\tau_0(\lambda))A(\lambda)}{1 - r(\tau_0(\lambda))A(\lambda)} \right\|^2 \quad (26)$$

with respect to AOT. This is possible if the phase function, single scattering albedo and the surface albedo are known in advance. However, this is not always the case. The following approach is often used in the retrievals (von Hoyningen-Huene et al., 2003; von Hoyningen-Huene et al., 2011; Katsev et al., 2010):

- (1) The phase function and single scattering albedo are assumed;
- (2) The spectra of soil and vegetation are prescribed (see Fig. 4);
- (3) The Angstrom law is assumed for the spectral AOT:

$$\tau_0(\lambda) = \tau_0(\lambda_0)(\lambda/\lambda_0)^{-\alpha}. \quad (27)$$

The parameters $\tau_0(\lambda_0)$, α and c are sought from a given set of spectral measurements $R_{mes}(\lambda)$. There are several weak points in this approach. In particular, it could be well the case that the assumed vegetation (or soil) spectra are not appropriate for a given region (say, over urban areas).

Then the approach based on the temporal satellite observations at a given location can be used. In particular, the minimal top-of-atmosphere reflectance as measured by an orbiting instrument is used to estimate the surface reflectance at a given location (Govaerts et al., 2009; Lyapustin and Wang, 2009).

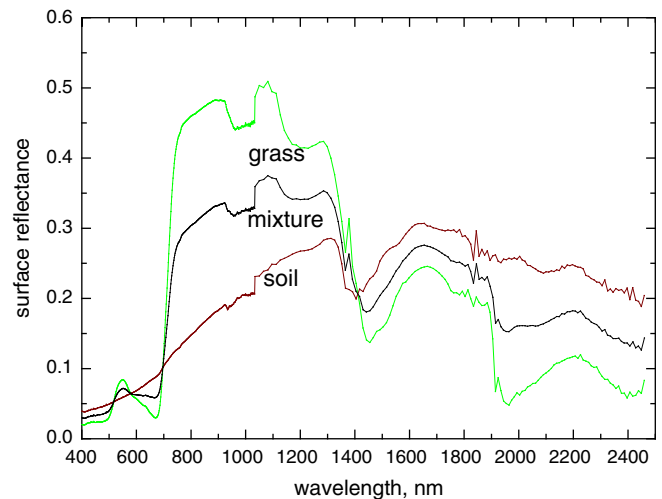


Fig. 4. The examples of spectral surface reflectance (A. Kuusk, private communication). The reflectance of mixed pixel was derived using linear mixing model with the vegetation fraction of 50%.

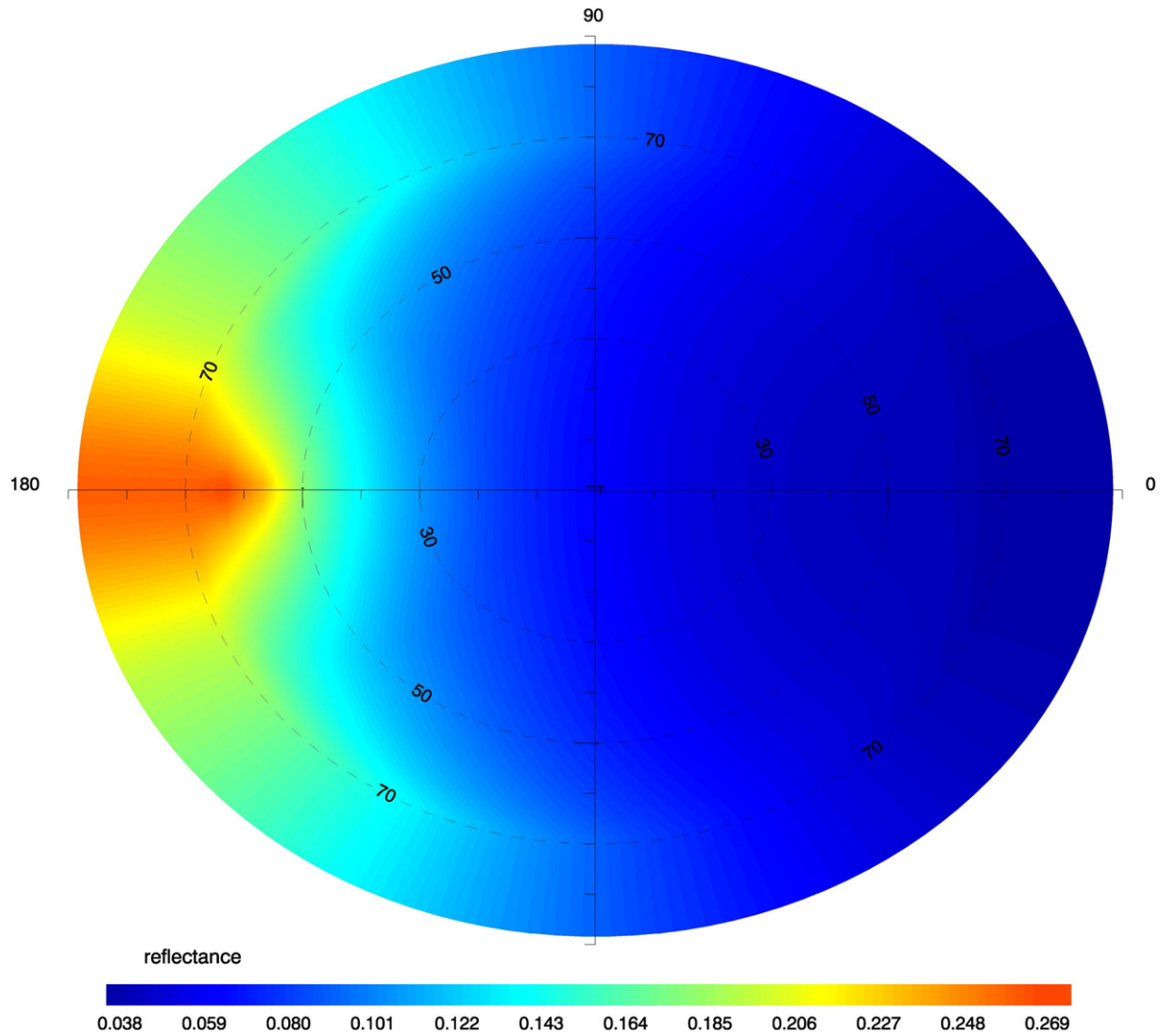


Fig. 5. The grass BRDF at 550 nm obtained using the model presented by Bréon and Vermote (2012).

In the case of double view or multi-angle observations, the Lambertian albedo can be removed from Eq. (20). So the exact value of A is not needed for the corresponding algorithm. In particular, we rewrite Eq. (20) in the following form:

$$A = \frac{R - R_b}{r(R - R_b) + t}. \quad (28)$$

This equation can be written for both views and used for the AOT retrievals assuming that A is the same for both views. Actually the algorithm works also for non-Lambertian surfaces under assumption that A can be presented as the product of the angular function (spectrally independent) and the spectral factor. Then for the case of low aerosol load, we may assume that (1) the aerosol does not make a contribution to the signal in the near infrared and (2) the unknown ratio of surface reflectances at two observation angles in the visible can be assessed from the measurements in the near-infrared.

The weak point of the algorithm is the fact that the underlying assumption of BRDF spectral invariance may not hold. Also Eq. (28) is valid only for Lambertian surfaces (Katsev et al., 2010; Zege et al., 2011).

More general approach is based on analytical models of the BRDFs. In particular, it is often assumed that R_s can be presented as

$$R_s = \kappa_0 \left[1 + \sum_{j=1}^L \kappa_j r_j \right], \quad (29)$$

where r_j are correspondent kernel functions and κ_j are spectrally dependent coefficients which describe the contribution of angular kernels to the overall signal (Rahman et al., 1993).

Various parameterizations of kernels are used (Dubovik et al., 2011) and the task of the retrieval algorithm is to find the aerosol optical thickness together with relevant parameters in kernels (and also functions $\kappa_j(\lambda)$).

3. Satellite instruments and algorithms used for aerosol optical thickness retrievals

3.1. Spectral top-of-atmosphere reflectance observations

A number of satellite instruments perform observation of a given atmospheric volume just at one observation angle. They include AVHRR, MODIS, MERIS, GLI, SEVIRI, and SeaWiFS among others. The

characteristics of the instruments are given in Table 1. SEVIRI is positioned on a geostationary satellite. Therefore, it can perform observations only in a well-defined area of the globe. This instrument has a capability to observe diurnal changes in aerosol properties (repetition time: 15 min), which is useful, e.g., in the detection of fires and the estimation of the trends in smoke extent.

Many instruments have similar choice of bands for the aerosol retrievals. Also algorithms do not differ considerably. The main idea is to find the aerosol model and spectral AOT, which gives the best fit of calculations and measurements (Gordon and Wang, 1994; Nakajima and Higurashi, 1997, 1998; King et al., 1999; Stamnes et al., 2003a,b).

In particular, the Moderate Resolution Imaging Spectroradiometer (MODIS) was launched in 1999 on board NASA TERRA satellite. An identical instrument flies on AQUA launched in 2004. The equator crossing time of TERRA is 10:30UTC (descending mode). It is 13:30UTC for AQUA (ascending mode). Although both instruments were initially the same, they degraded in a different way. MODIS has 36 channels from 0.41 till 15 μm with pixel sizes depending on the channel (see Table 1). The strong points of the instrument are due to broad spectral coverage, which enables the determination of various atmospheric and underlying surface parameters including aerosol and cloud optical thickness and surface BRDF. Weak points are due to the fact that the instrument has no capability of multi-angular and polarization measurements. So the information on aerosol for a given pixel is quite limited (at least, over land). The official Collection 5 MODIS algorithm operates in a different way over land and ocean. Over land, the algorithm relies on aerosol climatology (Levy, 2009). The following wavelengths are used in the retrieval process (over land): 0.47, 0.55, and 0.66 μm . The advantage of this approach is that the land surface reflectance is low at these channels (see Fig. 4). The disadvantage is due to the fact that rich spectral information contained in MODIS measurements is almost not used. In particular, the aerosol models are employed depending on the region. The look-up tables are built separately for fine (*f*) and coarse (*c*) modes. The aerosol reflectance is modeled as:

$$R = fR_f + (1-f)R_c, \quad (30)$$

where *f* is the fine mode fraction. The aerosol reflectance is obtained after correction for surface contribution, Rayleigh scattering and gaseous absorption effects. The task of the algorithm is to determine the fine mode fraction and combination of fine and coarse mode parameters, which provide the best fit. The surface reflectance is estimated using near infrared observations (e.g., 1.6 and 2.1 μm). It is assumed that the measurements at these channels are only slightly affected by aerosol and the surface albedo in the visible linearly depends on the surface albedo in the near infrared (with coefficients generally depending on the surface type (Levy, 2009)). The retrieval algorithms for the instruments, which have no capability to perform measurements in the near-infrared, are based either on the dark-pixel approach (*A*=0) or surface reflectance databases. In some cases they find a priori assumed vegetation/soil mixture parameter in a given pixel simultaneously with AOT retrieval (Kokhanovsky and de Leeuw, 2009). Yet another possibility is to study the relationship between the measured reflectances in the visible and near-infrared (Kaufman et al., 1997a,b). It is known that these reflectances are linearly dependent, if their surface reflectance counterparts are linearly correlated (Cahalan et al., 2001). Extrapolating the visible and near IR relation intercept, where the apparent reflectance of near IR reflectance is zero determines the path radiance at the visible bands, which can be used for the AOT retrieval. It is assumed then that the aerosol does not affect the top-of-atmosphere reflectance significantly in the near-IR, which is not always the case. Von Hoyningen-Huene et al. (2003) and Hsu et al. (2006) explored retrievals in the deep blue, where the surface contribution to the signal for many land surfaces is almost negligible.

Table 1

Channels of relevant aerosol remote sensing instruments (new channels as compared to heritage instruments are given in bold).

| Instrument | Channels | Comments |
|---|--|---|
| MODIS | 0.4125, 0.443, 0.469, 0.488, 0.531, 0.551, 0.555, 0.645, 0.667, 0.678, 0.748, 0.858, 0.8695, 0.905, 0.936, 0.940, 1.24, 1.375, 1.64, 2.13, 3.75, 3.959, 4.05, 4.465, 4.516, 6.715, 7.325, 8.55, 9.73, 11.03, 12.02, 13.335, 13.635, 13.935, and 14.235 μm | Bandwidth: 10–50 nm ($\lambda \leq 2.2 \mu\text{m}$) Spatial resolution: 0.25–1 km Swath: 2330 km |
| MERIS | 0.4125, 0.4425, 0.49, 0.51, 0.56, 0.62, 0.665, 0.68125, 0.705, 0.75375, 0.76, 0.775, 0.865, 0.89, and 0.9 μm | Bandwidth: 7.5–20 nm (3.75 nm at $\lambda = 760.625 \text{ nm}$) Spatial resolution: 0.3 km Swath: 1150 km |
| SeaWiFS | 0.412, 0.443, 0.49, 0.51, 0.555, 0.67, 0.765, and 0.865 μm | Bandwidth: 20 nm Spatial resolution: 1.1 km Swath: 2801 km |
| SEVIRI | 0.635, 0.81, 1.64, 3.92, 6.25, 7.35, 8.7, 9.66, 10.8, 12, and 13.4 μm | Bandwidth: 15–30 nm ($\lambda \leq 1.64 \mu\text{m}$) Spatial resolution: 0.25–1.0 km for most of channels Geostationary (15 min repetition time from 0° longitude) |
| GLI | 0.38, 0.4, 0.412, 0.443, 0.46, 0.49, 0.52, 0.545, 0.565, 0.625, 0.666, 0.68, 0.678, 0.71, 0.749, 0.763, 0.825, 0.865, 1.05, 1.135, 1.24, 1.38, 1.64, 2.21, 3.715, 6.7, 7.3, 8.6, 10.8, and 12 μm | Bandwidth: 10 nm ($\lambda \leq 0.865 \mu\text{m}$) Spatial resolution: 3.0 km for most of channels Swath: 1600 km |
| MSI (S2) 2012 ESA, Europe | 0.443, 0.490, 0.560, 0.665, 0.705, 0.740, 0.775, 0.842, 0.865, 0.940, 1.375, 1.61, and 2.19 μm | 13 bands 4 bands – 10 m 6 bands – 20 m 3 bands – 60 m Bandwidth: 20–115 nm Swath: 290 km |
| OLCI (S-3) 2013 ESA, Europe | 0.400, 0.412, 0.443, 0.490, 0.510, 0.560, 0.620, 0.665, 0.67375 , 0.68125, 0.70875, 0.75375, 0.76125, 0.76435 , 0.7675 , 0.77875, 0.865, 0.885, 0.900, 0.94 , and 1.02 μm | 21 bands All bands – 300 m Bandwidth: 2.5–40 nm Swath: 1300 km (5 cameras) |
| SLSTR (S-3) 2013 ESA, Europe | 0.555, 0.659, 0.865, 1.375 , 1.61, 2.25 , 3.74, 10.95, and 12.0 μm | 9 bands (dual-view) 6 bands – 500 m 3 bands – 1000 m (TIR) Bandwidth: 15–60 nm (0.38–1 μm in TIR) Swath: 1700 km (750 km for backward view) |
| TROPO-MI (S-5p) 2014 ESA, Europe | 270–495 nm 710–775 nm 2314–2382 nm | Hyperspectral (0.25–1.1 nm) Polar orbit Spatial resolution – 7 km Swath: 1700 km |
| UVN spectrometer (S-4) 2017 ESA, Europe | 305–400 nm 400–500 nm 750–775 nm | Hyperspectral (0.12–0.5 nm) Geostationary (60 min repetition time from 0° longitude), spatial resolution – 8 km, coverage: Europe (Sahara for calibration, southern and northern hemisphere can be pointed out) |
| ATLID (Earthcare) 2013 ESA-JAXA, Europe-Japan | 355 nm | Lidar system |

Table 1 (continued)

| Instrument | Channels | Comments |
|---|--|---|
| MSI (Earthcare) 2013 ESA-JAXA, Europe– Japan | 0.659, 0.865, 1.61, 2.2, 8.8, 10.8, and 12 μm | Bandwidth :0.02, 0.02, 0.06, 0.1, 0.9, 0.9, and 0.9 μm , respectively Spatial resolution : 500 m Swath : 150 km |
| VIIRS (NPP) 2011 NASA, USA | 0.412, 0.445, 0.488, 0.555, 0.64, 0.672, 0.7, 0.746, 0.865, 1.24, 1.378, 1.61, 2.25, 3.7, 4.05, 8.55, 10.673, 11.45, and 12.013 μm | Bandwidth: 15–60 nm (0.18–1.0 μm in TIR) Spatial resolution: 400–800 m Swath: 3000 km |
| S-GLI 2014 JAXA, Japan | 0.38, 0.412, 0.443, 0.490, 0.530, 0.565, 0.670, 0.763, 0.865, 1.05, 1.38, 1.64, 2.21, 10.8, and 12.0 μm | Bandwidth: 10–20 nm (0.05–0.7 μm in TIR) Spatial resolution: 250–1000 m Swath: 1400 km Channels 0.67 and 0.865 μm will also provide information on polarization characteristics of reflected light and perform multi-angular observations |

Over water, look-up-tables for MODIS retrievals are constructed at channels 0.47, 0.55, 0.66, 0.87, 1.2, 1.6, and 2.1 μm for several aerosol types and loadings, and illumination/viewing geometries. The algorithm picks up the best fine and coarse mode combinations, which minimize calculated and measured top of atmosphere reflectances. The solution includes the residual of the matches, which can be used to access the goodness of the solution. It should be emphasized that multiple solutions are possible because the solution of the inverse problem is poorly constrained (no angular and polarization measurements are available) for MODIS.

The results of global aerosol retrievals using MODIS are shown in Fig. 6. In particular, dust (yellow) and smoke (red) aerosols are clearly seen. The presence of heavy smoke aerosol in central Russia is due to unusually hot August in Moscow region in 2010. More detailed information on the aerosol spatial distribution can be deduced from the maps similar to that shown in Fig. 7 as derived from MERIS using BAER algorithm (von Hoyningen-Huene et al., 2003, 2011).

Other algorithms based on the spectral measurements use the target blurring method (Tanre, 1988) and cloud shadows (Duan et al., 2002).

3.2. Cloud screening

An important part of any aerosol retrieval algorithm is cloud screening (Bréon and Colzy, 1999; Zavody et al., 2000). The task is to identify pixels free of cloud contribution. The pixels must be clear both from presence of water droplets and also from the radiative influences of clouds (adjacency effects, cloud shadowing and clear sky brightness enhancements due to presence of nearby clouds).

Measurements in thermal infrared are traditionally used for cloud screening. This includes the reduced brightness temperature (BT) at 12 μm due to the presence of clouds (say, in upper cold atmospheric layers (Saunders and Kriebel, 1988)). Also the BT difference at 12 and 11 μm is analyzed to detect thin Cirrus clouds (Saunders and Kriebel, 1988; Kriebel et al., 2003).

The measurements in the absorption bands of atmospheric gases with high concentrations close to the ground (O_2 , CO_2 , and H_2O) are also used for cloud screening (Gao et al., 1998, 2002; Gao and Kaufman, 2003). The oxygen A-band (0.76 μm) and water vapor (1.38 μm) absorption bands are particularly useful. The physical basis of the method is simple. Indeed, reflectance is less reduced if clouds (even thin Cirrus) present over the analyzed ground scene. This increase in reflectance is due to the screening of trace gases in the lower atmosphere by clouds. The atmospheric gases absorb radiation at some characteristic bands and, therefore, reduce top-of-atmosphere reflectance. The methods also work for clouds over snow, where the channel at 1.6 μm can be used because generally clouds are much more reflective (smaller absorption by smaller ice grains and water droplets) as compared to snow in the near-infrared region of the electromagnetic spectrum.

Also one can use the fact that clouds are brighter as compared to most of ground scenes and are characterized by the reduced UV reflectance peak (due to the screening of scattering gaseous atmosphere under the clouds). Clouds produce strong rainbow seen in the intensity and degree of polarization. The identification of rainbow (or glory) with multi-angular and/or polarimetric observations also helps to distinguish clouds from a clear sky.

The statistical tests are often used as well (Gomez-Chova et al., 2007). In particular, the fact is used that the standard deviation of brightness temperature and reflectance is high for broken cloud fields. In some cloud screening algorithms, the retrieved AOT for most brightest and darkest pixels is rejected and then the average for the remaining pixels

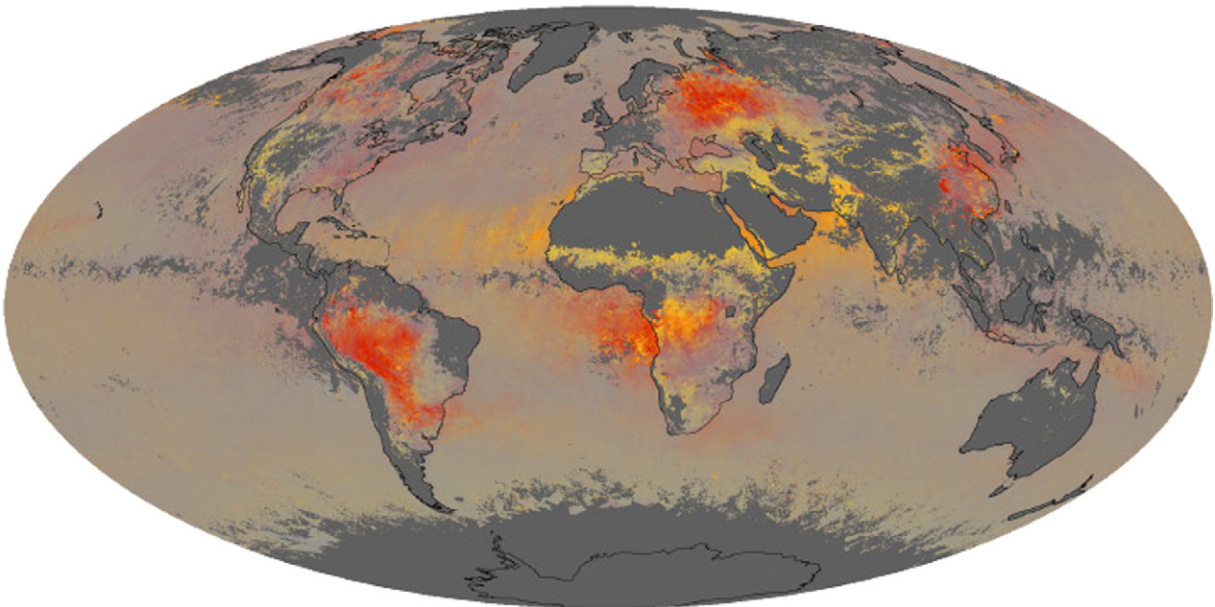


Fig. 6. The global distribution of smoke (red) and dust (yellow) aerosols in August 2010 as derived from MODIS (AQUA) data. Courtesy of NASA.

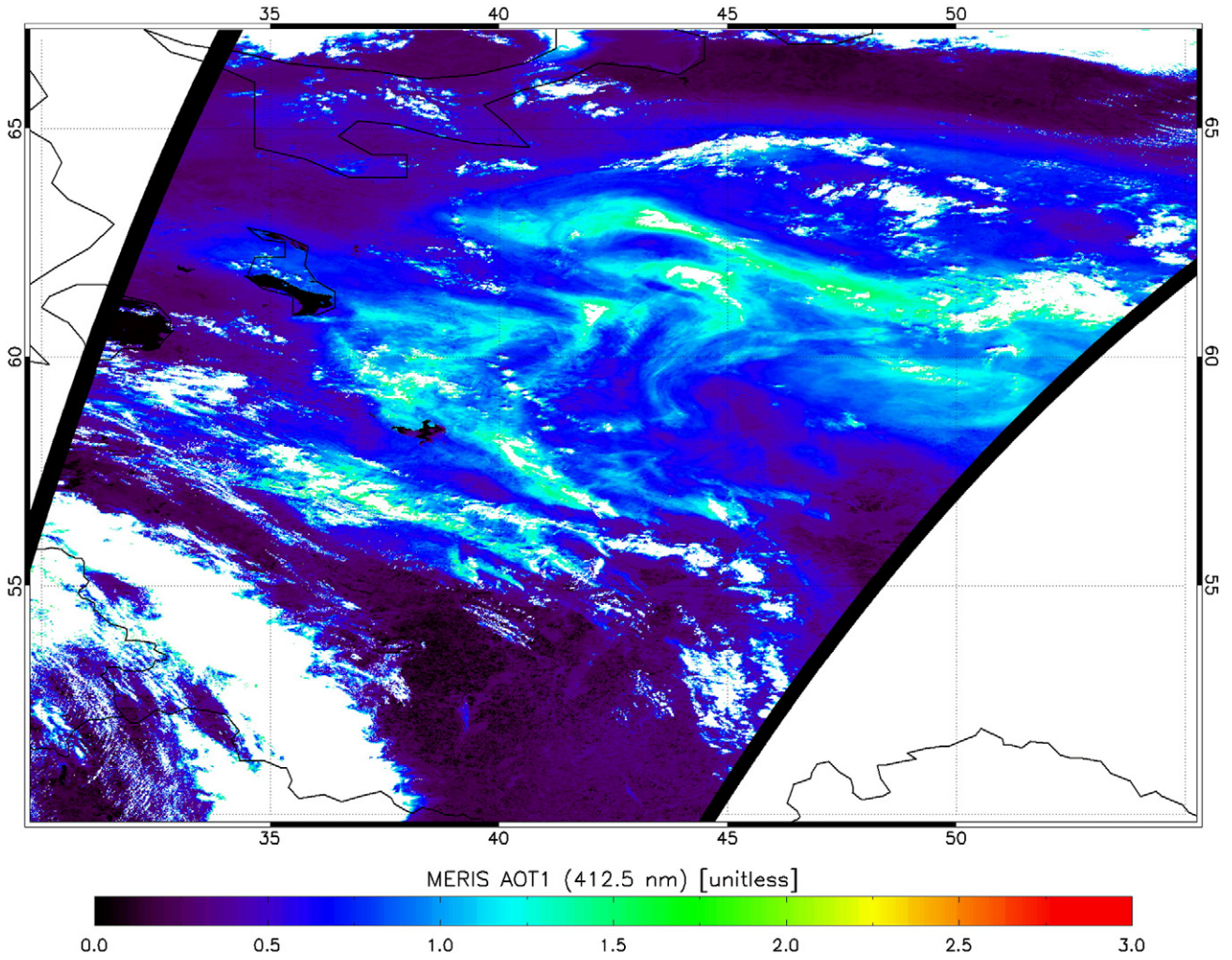


Fig. 7. The AOT (412.5 nm) as derived using MERIS measurements on July 29, 2010.

is used. This makes it possible to avoid effects related to cloud shadows and effects of radiative brightening of the nearby clear sky due to the presence of clouds, which act in some respect as non-perfect mirrors (if aerosol is observed at the region of sky from which solar light comes).

3.3. Dual view and multi-angular observations

3.3.1. AATSR

AATSR performs observations of the same scene at two views (0 and 55°) at the wavelengths 0.55, 0.66, 0.865, 1.6, 3.7, 11, and 12 μm (North et al., 1999; Thomas et al., 2009). IR channels help to enhance cloud screening algorithms (as compared, e.g., to MERIS and SeaWiFS). The most common AATSR retrieval approach is formulated as follows. Let us write Eq. (20) for forward (*f*) and nadir (*n*) views:

$$R_f = R_{bf} + \frac{t_f A}{1 - rA} \quad (31)$$

$$R_n = R_{bn} + \frac{t_n A}{1 - rA}. \quad (32)$$

One derives from these equations:

$$\frac{R_f - R_{bf}}{t_f} \frac{t_n}{R_n - R_{bn}} = \gamma, \quad (33)$$

where $\gamma = 1$ for ideal Lambertian surfaces. Eq. (33) can be used for the estimation of the spectral AOT. In practice, the value of γ (due to the fact that surface is usually non-Lambertian) is approximated by the ratio of reflectances (forward/nadir) at the wavelength 1.6 μm (assuming that $R_b \rightarrow 0$, $t \rightarrow 1$, and $r \rightarrow 0$ at 1.6 μm). This is possible because surface reflectance is due to scattering elements (say, leaves and grass), which are much larger than the wavelength and, therefore, γ can be considered as a spectrally independent parameter. An important point is the fact that Eq. (33) contains no surface parameters and, therefore, can be used to find AOT for an assumed phase function and single scattering albedo. Because measurements at several wavelengths are available, the aerosol model, which best fits multi-spectral and multi-angular observations, can be easily selected. The information on the aerosol model can be used to derive the surface spectral reflectance and, therefore, perform atmospheric correction, which is of great importance for the observation of land surfaces (e.g., different types of soil and crops) using space-borne instrumentation. Although the AATSR is better suitable for the removal of the surface contribution from the satellite signal as compared to MERIS, SeaWiFS, and MODIS, the problem of the separation of influences of AOT (aerosol load) and phase function (strength of scattering in a given direction) remains a challenge. The algorithm over ocean is similar to that of MODIS except both views are used in the fitting procedure. The example of retrievals for summer 2005 using AATSR is given in Fig. 8.

2005 June/July/August

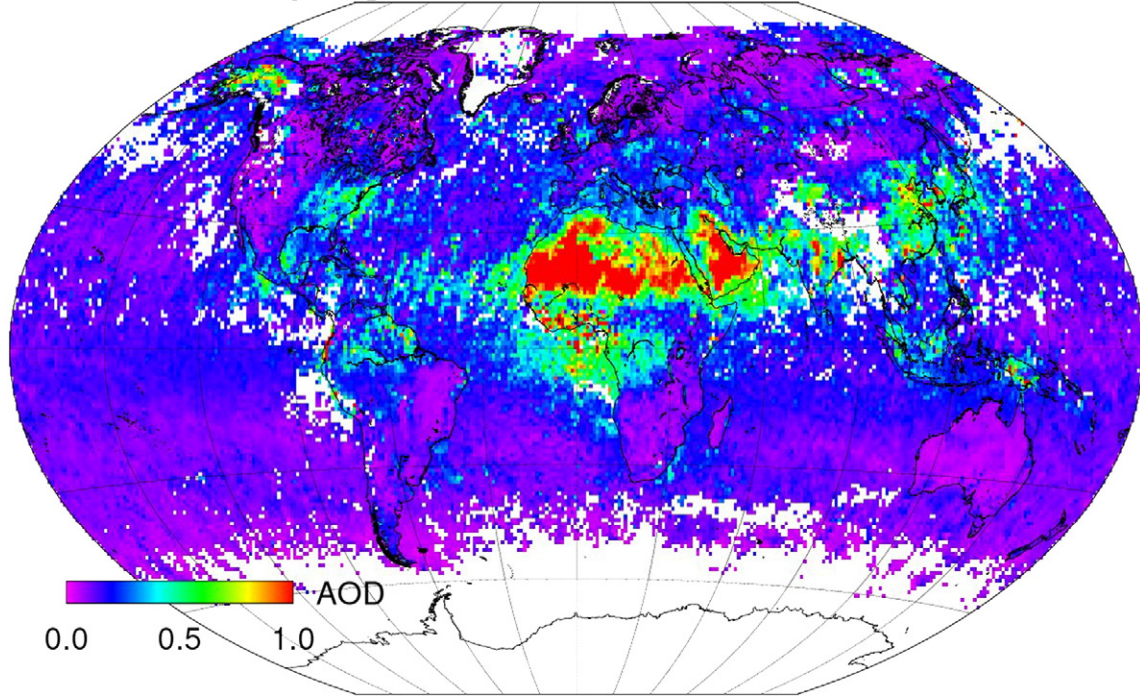


Fig. 8. The global map of AOT (550 nm) derived with AATSR for summer 2005 (Bevan et al., 2012).

3.3.2. MISR

MISR is NASA instrument operating on TERRA. Unlike AATSR it observes a given ground target simultaneously at 9 angles. Unfortunately, only channels at 446, 558, 672, and 866 nm are available, which reduces the cloud screening capability of the instrument. The spatial resolution is 275 m (250 m at the nadir observation). Therefore, small scale aerosol processes (local fires) are easily detected and quantified.

Because 9 equations (for each wavelength) and not 2 (as for AATSR) exist, the algorithm is capable to retrieve not only spectral AOT but also aerosol phase function (Diner et al., 2012). The spectral AOT is derived as a best fit after testing all MISR aerosol models and aerosol loads (the maximal AOT is 3.0 in the green band). If several aerosol models give a good fit passing an a priori defined criteria, then an appropriate model averaging procedure is applied (Martonchik et al., 1998). Because the number of MISR aerosol models is large, the reflectance is presented as a linear mixture of fine mode and coarse mode reflectances with corresponding coefficients determined during the retrieval process (Abdou et al., 1997).

MISR is also capable to determine aerosol plume height using stereoscopy (<http://www-misr.jpl.nasa.gov/getData/accessData/MisrMinxPlumes/>).

3.4. Multiangular spectropolarimetry

Without doubts, multi-angular polarimetric observations provide the best opportunity for the retrieval of aerosol properties from space (Mishchenko and Travis, 1997). Usually the Phillips–Tikhonov method or its modifications are applied in the retrievals (Dubovik et al., 2011; Hasekamp et al., 2011). Other minimization techniques are also used (Herman et al., 2005; Tanré et al., 2011). The Phillips–Tikhonov method finds the retrieved state vector by minimizing a cost function that is the sum of the least squares cost function and a side constraint weighted by the regularization parameter γ . Since the forward model is nonlinear with respect to the sought parameters, the inversion is carried iteratively.

For each iteration step, the forward model $\vec{\Phi}$ is replaced by its linear approximation (see, e.g., Hasekamp et al., 2011):

$$\vec{\Phi}(\vec{x}) = \vec{\Phi}(\vec{x}_n) + \hat{M}(\vec{x}_{n+1} - \vec{x}_n), \quad (34)$$

where \hat{M} is the Jacobian matrix containing the derivatives of the forward model with respect to the elements of the vector \vec{x} (e.g., sought parameters):

$$M_{ij} = \frac{\partial \phi_i}{\partial x_j}(\vec{x}_n). \quad (35)$$

The derivatives can be found numerically or analytically (e.g., the adjoint radiative transfer equation can be used (Rozañov et al., 2007)). The state vector is then found as

$$\vec{x}_{n+1} = \hat{G} \vec{y} + \hat{A} \vec{x}_n + (1 - \hat{A}) \vec{x}_a, \quad (36)$$

where $\hat{A} = \hat{G} \hat{K}$, $\hat{K} = \hat{S}_y^{-1/2} \hat{K} \hat{W}^{-1}$, $\hat{G} = (\hat{K}^T \hat{K} + \gamma \hat{I}) \hat{K}^T$, and $\vec{y} = \hat{S}_y^{-1/2} (\vec{Y} - \vec{\Phi}(\vec{x}_n))$.

Here \hat{I} is the unit matrix, \hat{W} is the weighting matrix (chosen to be diagonal such that $W_{ij} = x_{qj}^{-1}$), \hat{S}_y is the diagonal measurement error covariance matrix, which contains the measurement error estimate, $\vec{Y} = \vec{F}(\vec{x}) + \vec{e}_y$ is the measurement vector, which contains the observations of the polarimeter and \vec{e}_y is the error term.

For very thick aerosol layers (e.g., dust outbreaks close to the source), the value of AOT cannot be retrieved even using photopolarimetry because the layer acts effectively as a semi-infinite slab. The retrievals of the single scattering albedo and complex refractive index can be still performed, however (Kokhanovsky, 1999; Alakian et al., 2008).

3.5. Hyperspectral instruments

The hyperspectral measurements performed by a number of current instruments orbiting the planet are heavily underexplored as far as the determination of aerosol properties is of concern. The corresponding instruments are used mostly for the determination of trace gas concentrations based on the analysis of the strength of gaseous absorption bands (Burrows et al., 2011). The problem is due to the fact that these instruments observe large ground scenes and the measurements are often contaminated by clouds (Gottwald and Bovensmann, 2011). However, for clear cases aerosol properties can indeed be retrieved using algorithms similar to those employed by single view radiometers with advantages that measurements in the UV (as those performed by SCIAMACHY, OMI, and GOME-1 and 2) are not heavily influenced by the surface reflectance (the reflectance of most surfaces except snow is below 5% then, see Fig. 4). This is also the case for the measurements in the thermal IR, where there are channels for which radiation emitted by the surface does not reach the instrument due to the low transparency of atmosphere in corresponding channels (so retrievals above snow and ice and also at night are possible). The example of such an instrument is IASI, the Infrared Atmospheric Sounding Interferometer, which is a key payload element of the METOP series of European meteorological polar-orbit satellites. It is developed by CNES in the framework of a co-operation agreement with EUMETSAT. The first flight model was launched in 2006 onboard the first European meteorological polar-orbiting satellites, METOP-A. The second and third instruments will be mounted on the METOP-B and C satellites with launches scheduled in April 2012 and October–November 2016.

As a matter of fact, the hyperspectral measurements play a role of reflectance spectroscopy usually used in the lab to identify the chemical composition of a sample (see, e.g., Fig. 2 given by Clarisse et al., 2010). Yet another application of hyperspectral measurements is the determination of aerosol vertical distribution and aerosol layer height (Kokhanovsky and Rozanov, 2010). The technique is often used for the cloud top height determination (Koelemeijer et al., 2001; Rozanov and Kokhanovsky, 2004; Lelli et al., 2011) and based on the fact that the reflectance in the gaseous absorption bands (e.g., O_2 and CO_2) are strongly increased for cloudy scenes as compared to clear sky (due to screening of absorbing gas by a cloud). The retrievals are not so accurate as compared, e.g., to lidar-in-space systems. In principle, the synergy of hyperspectral and lidar measurements (currently under-explored) may enable better understanding aerosol vertical structure (especially for the area out of very narrow lidar footprint).

3.6. Spaceborne lidar systems

Spaceborne lidars provide information on the aerosol vertical structure and layering (see Fig. 1), which is almost missing in the passive systems discussed above. There were three successful lidar systems operated in space up to date. They are

- (1) Lidar In-space Technology Experiment (LITE, NASA, 1994, <http://www-lite.larc.nasa.gov>, channels: 355, 532, and 1064 nm);
- (2) Geoscience Laser Altimeter System (GLAS, NASA, 2003–2008, <http://glas.gsfc.nasa.gov>, channels: 532 and 1064 nm);
- (3) The Cloud-Aerosol Lidar and Infrared Pathfinder Satellite Observation (CALIPSO) satellite mission (CALIPSO, NASA, 2006–present, <http://www-calipso.larc.nasa.gov>, channels: 532, 532₊, and 1064 nm).

An important point is that unlike passive systems (with exclusion of IASI), space lidars provide information day and night because the system does not use solar light but rather lidar return signals from different aerosol layers. The instruments also provide almost direct measurements of AOT (under assumption of lidar ratio), which can

be used for the validation of AOTs retrieved using passive systems (Kittaka et al., 2011). Clearly, the lidar measurements are not affected by the underlying surface and can be performed over snow and ice. The global 3-D distribution of atmospheric aerosol as characterized by the CALIOP lidar, carried on the CALIPSO satellite, is presented by Winker et al. (2012).

4. Future missions

The aerosol remote sensing from space will be continued with the launch of new missions. The main characteristics of new instruments and the planned launch dates are given in Table 1. Let us characterize the capabilities of various future instruments with respect to the determination of aerosol optical properties.

Sentinel-2 will carry the Multispectral Imager (MSI). The expected lifetime is 7 years. It is planned that MSI will be launched on twin satellites on the same orbit, 180° apart one from the other. An important feature of this instrument is high spatial resolution (10–60 m) as needed for underlying surface remote sensing. Atmospheric correction can be performed using channels 0.74–2.19 μm over water and channels 0.443–0.665 μm over land. The channel at 1.375 μm can be used for Cirrus cloud screening. Generally, MSI aerosol retrieval algorithms can benefit from those of MODIS (Kokhanovsky and de Leeuw, 2009) because the setup of the visible – near IR wavelengths is similar to that of MODIS. In particular, over land one may use either approach based on the minimal reflectance or the correlation of ground reflectances with measurements at 1.61 and 2.19 μm , where atmospheric contribution is low.

Sentinel-3 will carry OLCI and SLSTR instruments, which observe the same area at the same time but have different pixel sizes and setup of channels. SLSTR has a capability to observe the same scene in the nadir view and also backwards (at the viewing zenith angle 55°). This feature enables more accurate AOT retrievals using the heritage algorithms of AATSR as explained above. The development of synergetic algorithms of SLSTR with OLCI equipped with 5 cameras and operating in the spectral range 0.4–1.2 μm is also possible. As compared to MERIS, OLCI has higher spectral resolution in the oxygen band, which can be used for better cloud screening and, possibly, for extracting some information on the position of aerosol layers in the atmosphere (Kokhanovsky and Rozanov, 2010). Generally, MERIS aerosol retrieval algorithms (Santer et al., 1999; Katsev et al., 2010; von Hoyningen-Huene et al., 2011) can be adapted for OLCI.

Sentinel 4 and 5 precursor is less suitable for aerosol remote sensing due to lack of several important channels and large size of ground scenes (50–60 km², see Table 1). Sentinel 4 will be placed on the geostationary orbit (at 0° longitude), which will make it possible to observe the aerosol (and trace gas) dynamics (e.g., fires, dust outbreaks, technological catastrophes, and volcanic eruptions with a repetition time of 1 h) in Europe. The hyperspectral capabilities of both instruments can be used for the vertical profiling of aerosol layers.

ATLID is the lidar in space, which will be launched on ESA-JAXA satellite Earthcare in 2013. The instrument will measure aerosol back-scattering at 350 nm and provide vertical structure of atmospheric aerosol. Earthcare will also carry MSI instrument with very limited capabilities for aerosol remote sensing over land. Over ocean, first four channels can be used.

VIIRS (NASA) and S-GLI (JAXA) will provide measurements at many channels previously available in MODIS. In addition, S-GLI has a capability of polarization measurements at 0.67 and 0.865 μm (together with multi-angular observations) and measurements at 0.38 μm , where underlying surface reflectance is small for almost all surfaces (except snow and ice). This will make it possible better characterization of aerosols. Also there is a good chance that NASA will launch polarimeter in space (as a substitution of failed GLORY mission). As it was underlined above, the multi-angular polarimetric measurements provide most accurate observations of atmospheric aerosol both from space and ground (Dubovik et al., 2011; Hasekamp et al., 2011).

5. Conclusions

Atmospheric remote sensing using space-borne observations (spectral, dual- and multiangular polarimetric) is a hot topic of modern atmospheric research. Currently, several aerosol retrieval algorithms are prepared and improved in major space agencies and remote sensing laboratories worldwide. There is no doubt that the launch of new instruments on space platforms during next 5 years will make it possible better characterization of global aerosol properties and their trends. An important point is the validation of retrievals using ground-based measurements (Holben et al., 1998; Sano et al., 2003; Smirnov et al., 2011) and also inter-comparison of retrievals as performed using different satellite instrumentation (Myhre et al., 2004; Kokhanovsky et al., 2007; Mishchenko et al., 2009; Kahn et al., 2010). The use of geostationary systems (see, e.g., Mei et al., 2012) will enable high temporal observations of aerosol load at specific locations important for monitoring (and prediction) of regional chemical weather and its change.

Acknowledgements

This work was supported by the DFG project Terra and also by the ESA CCI Project. The author is grateful to J. Yoon for the preparation of Fig. 7.

References

- Abdou, W., Martonchik, J., Kahn, R., West, R., Diner, D., 1997. A modified linear mixing method for calculating atmospheric path radiances of aerosol mixtures. *Journal of Geophysical Research* 102, 16883–16888.
- Alakian, A., Marion, R., Briottet, X., 2008. Remote sensing of aerosol plumes: a semianalytical model. *Applied Optics* 47, 1851–1866.
- Bevan, S.L., North, R.J., Los, S.O., Grey, W.M.F., 2012. A global dataset of atmospheric aerosol optical depth and surface reflectance from AATSR. *Remote Sensing of Environment* 116, 199–210.
- Bréon, F.-M., Colzy, S., 1999. Cloud detection from the spaceborne POLDER instrument and validation against surface synoptic observations. *Journal of Applied Meteorology* 38, 777–785.
- Bréon, F.-M., Vermote, E., 2012. Correction of MODIS surface reflectance time series for BRDF effects. *Remote Sensing of Environment* 125, 1–9.
- Burrows, J.P., Platt, U., Borell, P., 2011. *The Remote Sensing of Tropospheric Composition from Space*. Springer, Berlin.
- Cahalan, R.F., Oreopoulos, L., Wen, G., Marshak, A., Tsay, S.-C., DeFolice, T., 2001. Cloud characterization and clear-sky correction from Landsat-7. *Remote Sensing of Environment* 78, 83–98.
- Castanho, A.D.A., Vanderlei Martins, J., Artaxo, P., 2008. MODIS aerosol optical depth retrievals with high spatial resolution over an urban area using the critical reflectance. *Journal of Geophysical Research* 113, D02201. <http://dx.doi.org/10.1029/2007JD008751>.
- Clarisse, L., Hurtmans, D., Prata, A.J., Karagulian, F., Clerbaux, C., De Mazière, M., Coheur, P.-F., 2010. Retrieving radius, concentration, optical depth, and mass of different types of aerosols from high-resolution infrared nadir spectra. *Applied Optics* 49, 3713–3722.
- Diner, D.J., Hodos, R.A., Davis, A.B., Garay, M.J., Martonchik, J.V., Sanghavi, S.V., von Allmen, P., Kokhanovsky, A.A., Zhai, P., 2012. An optimization approach for aerosol retrievals using simulated MISR radiances. *Atmospheric Research* 116, 1–14.
- Duan, M., Lu, D., Cui, K., Hao, W., 2002. Retrieval of surface reflectance and aerosol optical thickness simultaneously from space measurements over land: basic theory and simulation. *Journal of Remote Sensing* 6 (5), 321–327.
- Dubovik, O., Herman, M., Holdak, A., Lapyonok, T., Tanré, D., Deuzé, J.L., Ducos, F., Sinyuk, A., Lopatin, A., 2011. Statistically optimized inversion algorithm for enhanced retrieval of aerosol properties from spectral multi-angle polarimetric satellite observations. *Atmospheric Measurement Techniques* 4, 975–1018.
- Gao, B.-C., Kaufman, Y., 2003. Water vapor retrievals using Moderate Resolution Imaging Spectroradiometer (MODIS) near-infrared channels. *Journal of Geophysical Research* 108, 4389.
- Gao, B.-C., Han, W., Tsay, S.C., Larsen, N.F., 1998. Cloud detection over Arctic region using airborne imaging spectrometer data during the daytime. *Journal of Applied Meteorology* 37, 1421–1429.
- Gao, B.-C., Kaufman, Y.J., Tanre, D., Li, R.R., 2002. Distinguishing tropospheric aerosols from thin cirrus clouds for improved aerosol retrievals using the ratio of 1.38 μm and 1.24 μm channels. *Geophysical Research Letters* 29, 1890. <http://dx.doi.org/10.1029/2002GL015475>.
- Gomez-Chova, L., Camps-Valls, G., Calpe, J., Guanter, L., Moreno, J., 2007. Cloud-screening algorithm for ENVISAT/MERIS multispectral images. *IEEE Transactions on Geoscience and Remote Sensing* 45, 4105–4118.
- Gordon, H.R., Wang, M., 1994. Retrieval of water-leaving radiances and aerosol optical thickness over the oceans with SeaWiFS: a preliminary algorithm. *Applied Optics* 33, 443–452.
- Gottwald, M., Bovensmann, H., 2011. *SCIAMACHY: Exploring the Changing Earth's Atmosphere*. Springer, Berlin.
- Govaerts, Y.M., Wagner, S., Lattanzio, A., Watts, P., 2009. Optimal estimation applied to the joint retrieval of aerosol optical depth and surface BRDF using MSG/SEVIRI observations. In: Kokhanovsky, A.A., de Leeuw, G. (Eds.), *Satellite Aerosol Remote Sensing Over Land*. Springer-Praxis, Berlin, pp. 327–360.
- Hasekamp, O.P., Litvinov, P., Butz, A., 2011. Aerosol properties over the ocean from PARASOL multiangle photopolarimetric measurements. *Journal of Geophysical Research* 116. <http://dx.doi.org/10.1029/2010JD015469>.
- Herman, M., Deuzé, J.-L., Marchand, A., Roger, B., Lallart, P., 2005. Aerosol remote sensing from POLDER/ADEOS over the ocean: Improved retrieval using a nonspherical particle model. *Journal of Geophysical Research* 110, D10S02. <http://dx.doi.org/10.1029/2004JD004798>.
- Holben, B.N., Eck, T.F., Slutsker, L., Tanré, D., Buis, J.P., Setzer, A., Vermote, E., Reagan, J.A., Kaufman, Y.J., Nakajima, T., Lavenu, F., Jankowiak, I., Smirnov, A., 1998. AERONET – a federated instrument network and data archive for aerosol characterization. *Remote Sensing of Environment* 66, 1–16.
- Hsu, N.C., Tsay, S.C., King, M.D., Herman, J.R., 2006. Deep blue retrievals of asian aerosol properties during ACE-Asia. *IEEE Transactions on Geoscience and Remote Sensing* 44, 3180–3195.
- Kahn, R.A., Gaitley, B.J., Garay, M.J., Diner, D.J., Eck, T.F., Smirnov, A., Holben, B.N., 2010. Multiangle Imaging SpectroRadiometer global aerosol product assessment by comparison with the Aerosol Robotic Network. *Journal of Geophysical Research* 115. <http://dx.doi.org/10.1029/2010JD014601>.
- Katsev, I.L., Prikhach, A.S., Zege, E.P., Grudo, J.O., Kokhanovsky, A.A., 2010. Speeding up the aerosol optical thickness retrieval using analytical solutions of radiative transfer theory. *Atmospheric Measurement Techniques* 3, 1403–1422.
- Kaufman, Y.J., Tanré, D., Remer, L., Vermote, E.F., Chu, A., Holben, B.N., 1997a. Operational remote sensing of tropospheric aerosol over the land from EOS-MODIS. *Journal of Geophysical Research* 102, 17051–17068.
- Kaufman, Y.J., Tanré, D., Gordon, H.R., Nakajima, T., Lenoble, J., Frouin, R., Grassl, H., Herman, B.M., King, M.D., Teillet, P.M., 1997b. Passive remote sensing of tropospheric aerosol and atmospheric correction for the aerosol effect. *Journal of Geophysical Research* 102, 16815–16830.
- King, M.D., Kaufman, Z.J., Tanre, D., Nakajima, T., 1999. Remote sensing of tropospheric aerosols from space: past, present, and future. *Bulletin of the American Meteorological Society* 80, 2229–2259.
- Kittaka, C., Winker, D.M., Vaughan, M.A., Omar, A., Remer, L.A., 2011. Inter-comparison of column aerosol optical depths from CALIPSO and MODIS-Aqua. *Atmospheric Measurement Techniques* 4, 131–141.
- Koelmeyer, R.B.A., Stammes, P., Hovenier, J.W., de Haan, J.D., 2001. A fast method for retrieval of cloud parameters using oxygen A-band measurements from the Global Ozone Monitoring Instrument. *Journal of Geophysical Research* 106, 3475–3490.
- Kokhanovsky, A.A., 1998. Variability of the phase function of atmospheric aerosols at large scattering angles. *Journal of Atmospheric Science* 55, 314–320.
- Kokhanovsky, A.A., 1999. On the determination of the refractive index of strongly absorbing particles in nonabsorbing host media. *Journal of Physics D: Applied Physics* 32, 825–831.
- Kokhanovsky, A.A., 2008. *Aerosol Optics*. Springer, Berlin.
- Kokhanovsky, A.A., de Leeuw, G. (Eds.), 2009. *Satellite Aerosol Remote Sensing Over Land*. Springer-Praxis, Berlin.
- Kokhanovsky, A.A., Rozanov, V.V., 2010. The determination of the dust cloud altitude from a satellite using hyperspectral measurements in the gaseous absorption band. *International Journal of Remote Sensing* 31, 2729–2744.
- Kokhanovsky, A.A., Breon, F.-M., Cacciari, A., Carboni, E., Diner, D.J., Di Nicolantonio, W., Grainger, R.G., Grey, W.M.F., Holler, R., Lee, K.-H., Li, Z., North, R.P.J., Sayer, A.M., Thomas, G.E., von Hoyningen-Huene, W., 2007. Aerosol remote sensing over land: a comparison of satellite retrievals using different algorithms and instruments. *Atmospheric Research* 85, 372–394.
- Koren, I., Remer, L.A., Kaufman, Y.J., Rudich, Y., Vanderlei Martins, J., 2007. On the twilight zone between clouds and aerosols. *Geophysical Research Letters* 34, L08805. <http://dx.doi.org/10.1029/2007GL029253>.
- Koren, I., Oreopoulos, L., Feingold, G., Remer, L.A., Altartaz, O., 2008. How small is a small cloud? *Atmospheric Chemistry and Physics* 8, 3855–3864.
- Kriebel, K.T., Gesell, G., Kästner, M., Mannstein, H., 2003. The cloud analysis tool APOLLO: improvements and validations. *International Journal of Remote Sensing* 24, 2389–2408.
- Lee, K.H., Li, Z., Kim, Y.J., Kokhanovsky, A.A., 2009. Atmospheric aerosol monitoring from satellite observations: a history of three decades. In: Kim, Y.J., Platt, U., Gu, M.B., Iwahashi, H. (Eds.), *Atmospheric and Biological Environmental Monitoring*, pp. 13–38.
- Lelli, L., Kokhanovsky, A.A., Rozanov, V.V., Vountas, M., Sayer, A.M., Burrows, J.P., 2011. Seven years of global retrieval of cloud properties using space-borne data of GOME-1. *Atmospheric Measurement Techniques Discussions* 4, 4991–5035.
- Levy, R., 2009. The dark-land MODIS collection 5 aerosol retrieval: algorithm development and product validation. In: Kokhanovsky, A.A., de Leeuw, G. (Eds.), *Satellite Aerosol Remote Sensing Over Land*. Springer-Praxis, Berlin, pp. 19–68.
- Lyapustin, A., Wang, Y., 2009. The time series technique for aerosol retrievals over land from MODIS. In: Kokhanovsky, A.A., de Leeuw, G. (Eds.), *Satellite Aerosol Remote Sensing Over Land*. Springer-Praxis, Berlin, pp. 69–100.
- Maignan, F., Breon, F.-M., Lacaze, R., 2004. Bidirectional reflectance of Earth targets: evaluation of analytical models using a large set of spaceborne measurements with emphasis on the Hot Spot. *Remote Sensing of Environment* 90, 210–220.
- Martonchik, J.V., Diner, D.J., Kahn, R.A., Ackerman, T.P., Verstraete, M.M., Pinty, B., Gordon, H.R., 1998. Techniques for the retrieval of aerosol properties over land and ocean using multiangle imaging. *IEEE Transactions on Geoscience and Remote Sensing* 36, 1212–1227.

- Mei, L., Xue, Y., de Leeuw, G., Holzer-Popp, T., Guang, J., Li, Y., Yang, L., Xu, H., Xu, X., Li, C., Wang, Y., Wu, C., Hou, T., He, X., Liu, J., Dong, J., Chen, Z., 2012. Retrieval of aerosol optical depth over land based on a time series technique using MSG/SEVIRI data. *Atmospheric Chemistry and Physics* 12, 9167–9185.
- Mishchenko, M.I., Travis, L.D., 1997. Satellite retrieval of aerosol properties over the ocean using polarization as well as intensity of reflected sunlight. *Journal of Geophysical Research* 102, 16989–17013.
- Mishchenko, M.I., Geogdzhayev, I.V., Liu, L., Lacis, A.A., Cairns, B., Travis, L.D., 2009. Toward unified satellite climatology of aerosol properties: what do fully compatible MODIS and MISR aerosol pixels tell us? *Journal of Quantitative Spectroscopy and Radiative Transfer* 110, 402–408.
- Myhre, G., Stordal, F., Johnsrud, M., Ignatov, A., Mishchenko, M.I., Geogdzhayev, I.V., Tanré, D., Deuzé, J.-L., Goloub, P., Nakajima, T., Higurashi, A., Torres, O., Holben, B.N., 2004. Intercomparison of satellite retrieved aerosol optical depth over the ocean. *Journal of Atmospheric Science* 61, 499–513.
- Nakajima, T., Higurashi, A., 1997. AVHRR remote sensing of aerosol optical properties in the Persian Gulf region, the summer, 1991. *Journal of Geophysical Research* 102, 16935–16946.
- Nakajima, T., Higurashi, A., 1998. A use of two-channel radiances for an aerosol characterization from space. *Geophysical Research Letters* 25, 3815–3818.
- North, R.P., Briggs, S.A., Plummer, S.E., Settle, J.J., 1999. Retrieval of land surface bidirectional reflectance and aerosol opacity from atsr-2 multiangle imagery. *IEEE Transactions on Geoscience and Remote Sensing* 37, 526–537.
- Pinty, B., Roveda, F., Verstraete, M., Gobron, N., Govaerts, Y., Martonchik, J., Diner, D.J., Kahn, R., 2000. Surface albedo retrieval from Meteosat 1. Theory. *Journal of Geophysical Research* 105. <http://dx.doi.org/10.1029/2000JD900113>.
- Rahman, H., Pinty, B., Verstraete, M., 1993. Coupled surface atmosphere reflectance (CSAR) model, 2, Semiempirical surface model usable with NOAA Advanced Very High Resolution Radiometer data. *Journal of Geophysical Research* 98, 20,791–20,801.
- Rohen, G.J., von Hoyningen-Huene, W., Kokhanovsky, A., Dinter, T., Vountas, M., Burrows, J.P., 2011. Retrieval of aerosol mass load (PM_{10}) from MERIS/Envisat top of atmosphere spectral reflectance measurements over Germany. *Atmospheric Measurement Techniques* 4, 523–534.
- Rozanov, V.V., Kokhanovsky, A.A., 2004. The semi-analytical cloud retrieval algorithm as applied to the cloud top altitude and the cloud geometrical thickness determination from the top of atmosphere reflectance measurements in the oxygen absorption bands. *Journal of Geophysical Research* 109. <http://dx.doi.org/10.1029/2003JD004104>.
- Rozanov, V.V., Rozanov, A.V., Kokhanovsky, A.A., 2007. Derivatives of the radiation field and their application to the solution of inverse problems. *Light Scattering Reviews*, 2. Springer, Berlin.
- Rozanov, V.V., Rozanov, A.V., Kokhanovsky, A.A., Burrows, J.P., in preparation. SCIATRAN – a software package for the simulation of radiative transfer in atmosphere. *Journal of Quantitative Spectroscopy and Radiative Transfer*.
- Sano, I., Mukai, S., Yamano, M., Takamura, T., Nakajima, T., Holben, B., 2003. Calibration and validation of retrieved aerosol properties based on Aeronet and Skynet. *Advances in Space Research*. [http://dx.doi.org/10.1016/S0273-1177\(03\)00685-9](http://dx.doi.org/10.1016/S0273-1177(03)00685-9), 2159–2164.
- Santer, R., Carrere, V., Dubuisson, P., Roger, J.C., 1999. Atmospheric correction over land for MERIS. *International Journal of Remote Sensing* 20, 1819–1840.
- Saunders, R.W., Kriebel, K.T., 1988. An improved method for detecting clear sky and cloudy radiances from AVHRR data. *International Journal of Remote Sensing* 9, 123–150.
- Seidel, F., Kokhanovsky, A.A., Schaepman, M.E., 2012. Fast retrieval of aerosol optical depth and its sensitivity to surface albedo using remote sensing data. *Atmospheric Research* 116, 22–32.
- Smirnov, A., Holben, B.N., Giles, D.M., Slutsker, I., O'Neill, N.T., Eck, T.F., Macke, A., Croot, P., Courcoux, Y., Sakerin, S.M., Smyth, T.J., Zielinski, T., Zibordi, G., Goes, J.I., Harvey, M.J., Quinn, P.K., Nelson, N.B., Radionov, V.F., Duarte, C.M., Losno, R., Sciarre, J., Voss, K.J., Kinne, S., Nalli, N.R., Joseph, E., Krishna Moorthy, K., Covert, D.S., Gulev, S.K., Milinevsky, G., Larouche, P., Belanger, S., Horne, E., Chin, M., Remer, L.A., Kahn, R.A., Reid, J.S., Schulz, M., Heald, C.L., Zhang, J., Lapina, K., Kleidman, R.G., Griesfeller, J., Gaitley, B.J., Tan, Q., Diehl, T.L., 2011. Maritime aerosol network as a component of AERONET – first results and comparison with global aerosol models and satellite retrievals. *Atmospheric Measurement Techniques* 4, 583–597.
- Sobolev, V.V., 1975. *Light Scattering in Planetary Atmospheres*. Nauka, Moscow.
- Stamnes, K., Li, W., Yan, B., Eide, H., Barnard, W., Pegau, S., Stamnes, J.J., 2003a. Accurate and self-consistent ocean color algorithm: simultaneous retrieval of aerosol optical properties and chlorophyll concentrations. *Applied Optics* 42, 939–951.
- Stamnes, K., Yan, B., Li, W., Stamnes, J.J., Tsay, S.-C., 2003b. Pitfalls in atmospheric correction of ocean color imagery: how should aerosol optical properties be computed?: reply to comment. *Applied Optics* 42, 545–549.
- Tanre, D., 1988. Estimation of Saharan aerosol optical thickness from blurring effects in thematic mapper data. *Journal of Geophysical Research* 93 (D12), 15955–15964.
- Tanré, D., Bréon, F.M., Deuzé, J.L., Dubovik, O., Ducos, F., François, P., Goloub, P., Herman, M., Lifermann, A., Waquet, F., 2011. Remote sensing of aerosols by using polarized, directional and spectral measurements within the A-Train: the PARASOL mission. *Atmospheric Measurement Techniques Discussions* 4, 2037–2206.
- Thomas, G.E., Poulsen, C.A., Sayer, A.M., Marsh, S.H., Dean, S.M., Carboni, E., Siddans, R., Grainger, R.G., Lawrence, B.N., 2009. The GRAPE aerosol retrieval algorithm. *Atmospheric Measurement Techniques* 2, 679–701.
- van Zelm, R., Huijbregts, M.A.J., den Hollander, H.A., van Jaarsveld, H.A., Sauter, F.J., Struijs, J., van Wijnen, H.J., van de Meent, D., 2008. European characterization factors for human health damage of PM_{10} and ozone in life cycle impact assessment. *Atmospheric Environment* 42, 441–453.
- von Hoyningen-Huene, W., Freitag, M., Burrows, J.B., 2003. Retrieval of aerosol optical thickness over land surfaces from top-of-atmosphere radiance. *Journal of Geophysical Research* 108, 4260. <http://dx.doi.org/10.1029/2001JD002018>.
- von Hoyningen-Huene, W., Yoon, J., Vountas, M., Istomina, L.G., Rohen, G., Dinter, T., Kokhanovsky, A.A., Burrows, J.P., 2011. Retrieval of spectral aerosol optical thickness over land using ocean color sensors MERIS and SeaWiFS. *Atmospheric Measurement Techniques* 4, 151–171.
- Winker, D.M., Tackett, J.L., Getzewich, B.J., Liu, Z., Vaughan, M.A., Rogers, R.R., 2012. The global 3-D distribution of tropospheric aerosols as characterized by CALIOP. *Atmospheric Chemistry and Physics Discussions* 12, 24847–24893.
- Zavody, A.M., Mutlow, C.T., Llewellyn-Jones, D.T., 2000. Cloud clearing over the ocean in the processing of data from the Along-Track Scanning Radiometer (ATSR). *Journal of Atmospheric and Oceanic Technology* 17, 595–615.
- Zege, E.P., Katsev, I.L., Malinka, A.V., Prikhach, A.S., Heygster, G., Wiebe, H., 2011. Algorithm for retrieval of the effective snow grain size and pollution amount from satellite measurements. *Remote Sensing of Environment* 115, 2674–2685.